CMS Physics Analysis Summary

Contact: cms-pog-conveners-tracking@cern.ch 2010/07/29

Studies of Tracker Material

The CMS Collaboration

Abstract

In this Analysis Summary, we present initial results of two complementary studies of the distribution and the effects of material within the CMS Tracker. The first is based on the reconstruction of secondary vertices resulting from photon conversions and nuclear interactions within the material inside the tracking volume; the second is based on the determination of multiple scattering through the material in the tracking volume. Preliminary results obtained with the first 7TeV data of 2010 are shown. The agreement between data and simulation is typically in the 10% range.

1 Introduction

The Compact Muon Solenoid (CMS) [1] is one of two general-purpose detectors operating at the Large Hadron Collider (LHC) facility at CERN. One of the central features of the CMS detector is a 6-m diameter solenoidal magnet operating at 3.8 T, which enables the measurement of charged particle momenta over more than four orders of magnitude, from less than 100 MeV/c to more than 1 TeV/c, by reconstructing their trajectories as they traverse the CMS inner tracking system. The CMS Tracker, shown in Fig. 1, consists of two main detectors: three barrel layers and two endcap disks per side of silicon pixel detectors, covering the region from 4 cm to 15 cm in radius, and within 49 cm on either side of the collision point along the LHC beam axis; ten barrel layers and twelve endcap disks per side of silicon strip detectors, covering the region from 25 to 110 cm in radius, and within 280 cm on either side of the collision point along the LHC beam axis. The Tracker acceptance extends up to a pseudo-rapidity of $|\eta| < 2.5$.

The CMS experiment uses a right-handed coordinate system, with the origin at the nominal interaction point, the x axis pointing to the centre of the LHC ring, the y axis pointing up (perpendicular to the LHC plane) and the z axis along the anticlockwise-beam direction. The azimuthal angle ϕ is measured in the x-y plane, with $\phi = 0$ along the positive x axis and $\phi = \pi/2$ along the positive y axis and the radial coordinate in this plane is denoted by R. The polar angle θ is measured from the z axis. Pseudo-rapidity is defined as $\eta = -\ln\tan(\theta/2)$.

The precise and efficient determination of charged-particle momenta is a critical component of the physics program of CMS, as it impacts the ability to reconstruct leptons, charged hadrons, jets, and photon conversions, which are the basic physics objects needed to understand pp collisions at the LHC. Standard reconstruction of tracks in the CMS Tracker is seeded by the hits in the detector [2]. Seeds are then propagated outward, adding compatible hits and updating the trajectory until either the detector boundary is reached, or no additional compatible hits can be found. In the final stage, the collection of hits is fit to obtain the best estimate of the track parameters.

Material within the tracking volume, however, affects the overall event topology, reconstruction and analysis, through electron bremsstrahlung, photon conversions and nuclear interactions. It also affects the trajectories of charged tracks because of multiple scattering and energy loss.

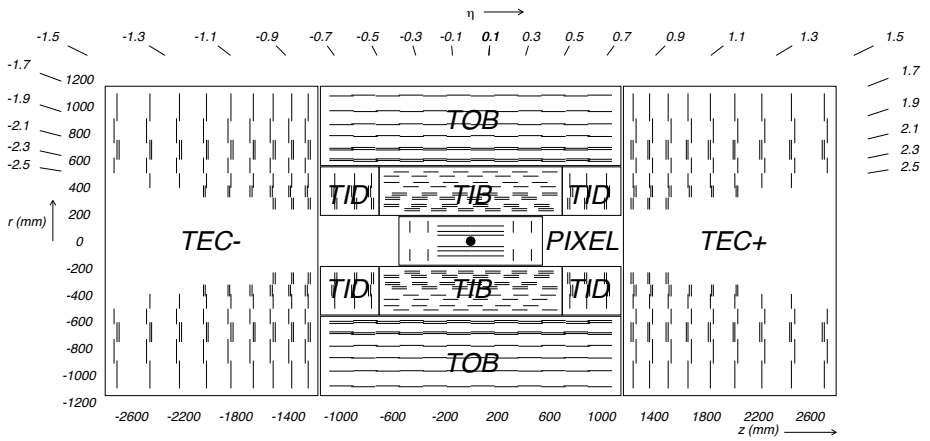

Figure 1: Schematic cross section of the CMS Tracker.

A correct simulation of all these effects is required for a well-understood track and event reconstruction, and a substantial effort has been invested in generating a detailed GEANT4 [3, 4] geometry used to simulate data samples [5]. For a discussion of the systematic uncertainties related to the Tracker material simulation, not addressed here, see [6].

In this Analysis Summary, we present studies of photon conversions, nuclear interactions and multiple scattering and their use to check the consistency of the Tracker simulation geometry with the material distribution inside the actual detector.

In Section 2 we summarize the data sets used in the analyses presented here. In Section 3 an improvement to the track seeding instrumental to this work is described. In Sections 4 and 5 the reconstruction of photon conversions and nuclear interactions in the Tracker is presented. In Section 6 photon conversions and nuclear interactions are used to probe the material in the tracking volume, and to check the accuracy of the geometry implemented in the Tracker simulation. In Section 7 a study of charged particles multiple scattering is presented, which is in turn used to check the accuracy of the Tracker simulation geometry. Finally conclusions are drawn in Section 8.

2 Data and simulation samples

If not differently specified the samples used for the present work are the following.

Data. The list of analyzed sets of data is taken from the centrally produced table of all runs at 7 TeV with detector in stable conditions and magnet fully operational, collected up to 6 May 2010, for a total integrated luminosity of $1.0 \pm 0.1\text{nb}^{-1}$.

Monte Carlo simulation. A sample of $\sim$ 50M events of minimum bias at 7 TeV is used; this sample is generated with PYTHIA6.4 [7] and processed with a simulation of the CMS detector response based on GEANT4. The misalignment, mis-calibrations and dead channel map corresponding to the detector status and calibration accuracy have been included in the simulation. Both longitudinal and transverse coordinates of the primary collision vertices has been tuned to match the real data.

Events are selected if the following criteria are satisfied.

Trigger requirements. All the sub-detectors must be on; the coincidence of any *Beam Scintillator Counter* (BSC) hit with a signal from both *Beam Pick-up Timing for experiment's* (BPTX) stations is required, in addition with a veto from the beam-halo trigger. The BSC [8] are scintillator counters placed around the beam pipe in the forward regions. The two BPTX [9] stations are electrostatic pickups installed on the two sides of the detector, at about 175 m from the interaction point. Events containing beam-halo muons crossing the detector were identified and rejected by requiring the time difference between any two hits from the BSC stations on opposite sides of the interaction points to fall within a 73 ± 20 ns time window.

Beam background event rejection. Beam-induced background events, producing an anomalously large number of hits in Pixel detector, are rejected by requiring the fraction of high purity tracks in the event to exceed 20% [2].

A *good* reconstructed primary vertex. A reconstructed primary vertex is defined as good if at least four tracks are originating from it and if its position lies within 15 cm in the longi-

tudinal direction and within 2 cm in the transverse plane with respect to the beam spot centre.

In total $\sim$ 25 millions events survive the event selection in the analysed data sample, and $\sim$ 29 millions in the simulation sample.

3 Tracking improvements

The detection of photon conversions and nuclear interactions both rely on the reconstruction of displaced secondary vertices, and the track reconstruction algorithm described in [2] has been tuned to allow reconstruction of tracks originated into the tracking volume, as far as at a radius of 60 cm.

The standard CMS tracking is made of six iterative steps, numbered from 0 to 5, designed to obtain high efficiency and low fake rate for tracks coming either from the primary vertex or from displaced decay vertices while maintaining the overall computing time within the requirements of CMS offline reconstruction centre. Because of this constraint, the standard implementation is not optimal to reconstruct with high efficiency tracks from photon conversions and nuclear interactions since the cuts applied in the standard reconstruction are too tight for these processes. In fact, those tracks have usually very low momentum and, especially for displaced vertices at large radii, they do not point back to the primary vertex; therefore, they could be reconstructed only with very relaxed cuts that would result into unacceptably large computing time during the pattern recognition.

For the purpose of the present study, two additional dedicated tracking steps are added to the track reconstruction sequence. These were specifically designed to increase the number of reconstructed conversion vertices in the barrel region, but they have been found to be very useful for nuclear interaction as well. A first additional step (step 6) is seeded from triplets of hits in the Pixel barrel and/or in the Strip Tracker Inner barrel detectors; a second additional step (step 7) is seeded from hit-pairs in the Strip Tracker barrel detectors and/or in the Strip Tracker Inner disks. The seed trajectories are required to have a minimum transverse momentum of 0.1 and 0.2 GeV/c for the step 6 and 7, respectively. The resulting large number of seeds is reduced by selecting topologies compatible with a photon conversion pair: the total charge has to be zero, the azimuthal angle difference less than 1.5 radians, the difference in the cotangent of the polar angle less than 0.25 radians, and the differences of the radial and longitudinal coordinates of the innermost hit have to be less then 5 cm. The pattern recognition is then performed allowing for at most one lost hit and requiring at least three hits. Finally the standard track fit provides the best estimate of the track parameters.

The impact of the additional steps to the reconstruction of conversion and nuclear interaction vertices can be seen on Fig. 2 showing the contribution of the different steps to the vertices reconstruction, as estimated by the simulation. Step 7 increases by more than a factor two the number of conversions outside the Pixel detector region and contributes significantly to nuclear interaction vertices at all radii; step 6 mainly helps finding conversions in the second and third Pixel detector layers. Further details about the reconstruction of conversions and nuclear interactions will be given in the following sections.

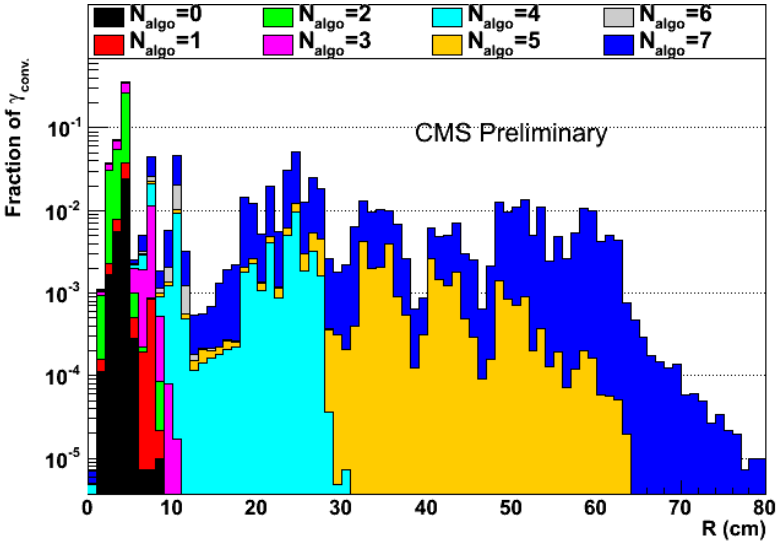

(a)

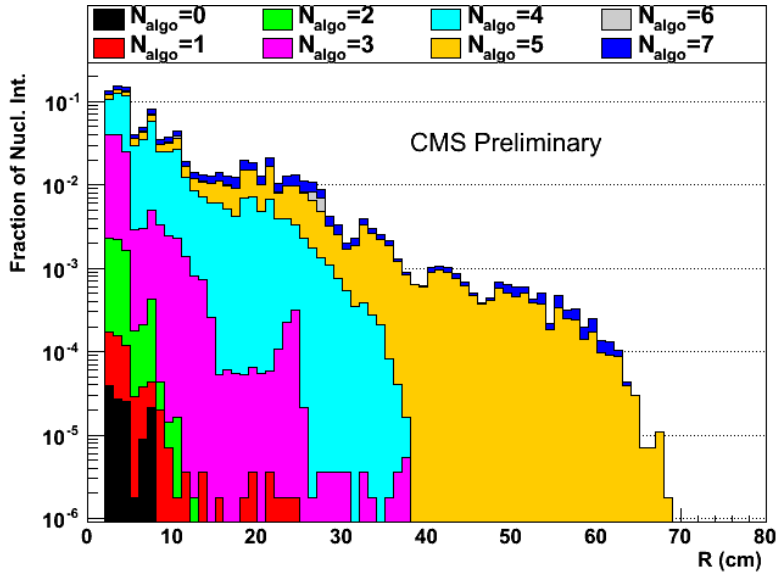

(b)

Figure 2: Fraction of reconstructed vertices as a function of the radius of the vertex for conversions (a) and nuclear interactions (b), for $|\eta| < 1.4$, as estimated from simulation. The different colors correspond to the largest iterative step needed to reconstruct the tracks at the vertex.

4 Photon Conversion Reconstruction

Up to 70% of photons traversing the Tracker material converts into e^+e^- pairs. In the Minimum Bias events collected during the first phase of CMS data taking, photons, mainly coming from π^0 decays, are expected to have a very soft spectrum. The electron pairs from conversions are very unlikely to reach the Electromagnetic Calorimeter (ECAL) and the ECAL cluster-driven track and seed finding method [10, 11] cannot be applied. The development of the iterative tracking described in [2] largely extended the capability of reconstructing low-p_{T} tracks and displaced vertices. Furthermore, for the work presented in this Analysis Summary, additional seeding steps were introduced as described in Sec. 3 and exploited here to improve the identification of conversions at large radii. The tracker-only conversion reconstruction was already partially commissioned with limited statistics during the LHC runs at $\sqrt{s} = 900\,\mathrm{GeV}$ data [2].

Photon conversions are characterized by a pair of oppositely charged secondary tracks, originating from the photon vertex with an invariant mass consistent with zero, which are therefore parallel to each other at production vertex. The electron-positron pair, then, opens only in the transverse plane because of the solenoidal magnetic field.

The tracker-driven conversion reconstruction is based on a simple track pair pre-selection already described in [2]. We summarize the method here mentioning the changes with respect to [2]. Opposite-sign track pairs are firstly required to satisfy basic quality criteria, i.e. have ≥ 6 hits and normalised $\chi^2 < 10$. Then the tracker-only conversion finding exploits the conversion pair signature to distinguish genuine pairs from fake pairs. Tracks are required to have positive charge-signed transverse impact parameter (the primary vertex lies outside the track trajectory helix) and the distance of minimum approach in 2D, d_m, between $-0.25\,\mathrm{cm}$ and $1\,\mathrm{cm}$. As sketched in Fig. 3 for the positive and negative case, d_m is defined as $d_{O_1-O_2} - (R_1 - R_2)$ where $d_{O_1-O_2}$ is the distance between the centres of the two track circles in the transverse plane and R_1 and R_2 are the two circles radii.

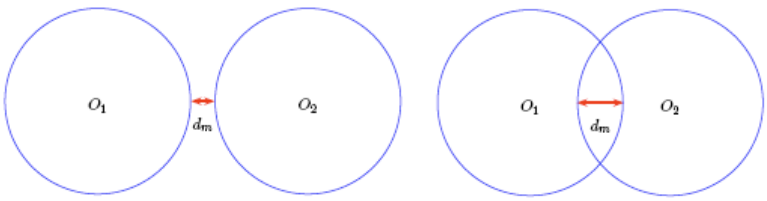

(a) (b)

Figure 3: Example of a positive (a) and a negative (b) distance of minimum approach between two ideal track circles.

Further requirements include a small z separation between the tracks innermost points ($|\Delta z| < 5\,\mathrm{cm}$) if they are in the barrel ($|z| < 120\,\mathrm{cm}$) and a small opening angle in the longitudinal plane ($|\Delta \cot\theta| < 0.1$). Track pairs surviving the selection are then fitted to a common 3D-constrained kinematic vertex fitter. The 3D constraints imposes the tracks to be parallel in both transverse and longitudinal planes. The pair is retained if the fit converges and its χ^2 probability is greater than 5×10^{-4}. The addition with respect to [2] of the requirement that both tracks have a transverse momentum $\mathrm{P}_T > 0.5\,\mathrm{GeV}/c$ reduces significantly the amount of fake pairs. The total number of conversion candidates reconstructed in data is about 260 thousands.

The contribution from fake conversions is estimated from simulated data; true conversions are identified by accessing the simulated photon vertex and the electron tracks originating from it.

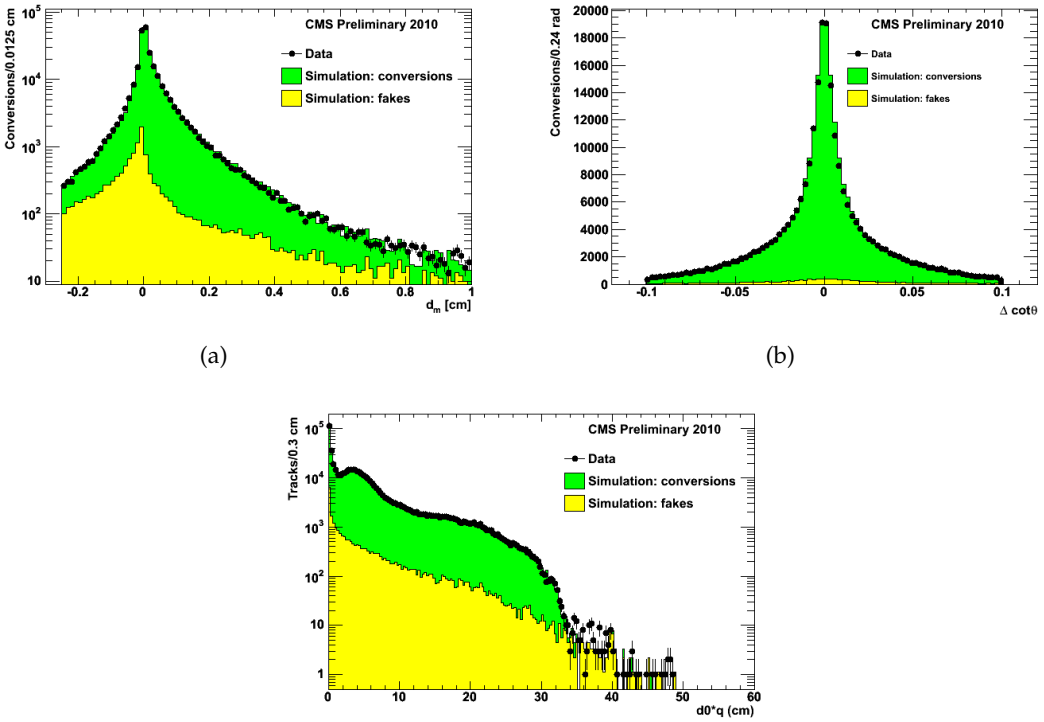

Figure 4: Distance of minimum approach, d_m, between the electron tracks (a), angular separation in the longitudinal plane, $\Delta \cot\theta$, of tracks (b), and charge-signed transverse track impact parameter (c). The expected contribution from fakes is also shown.

Reconstructed conversions in simulated data are matched to true conversions by checking the vicinity of the vertex position, i.e. requiring that each vertex coordinate is within 5 cm (10 cm) from the truth, for $|\eta| < 1.2$ ($|\eta| > 1.2$).

Figure 4 shows very good agreement between data and simulation for some of the discriminating variables used in the selection. In all plots, the normalisation is to the number of entries in data after the cuts. Figure 5 shows the χ^2 probability of the final constrained vertex fit after applying all cuts, including the one on the probability itself. A post-fit check is performed using the original (i.e. non refitted with the vertex constraint) conversion tracks, extrapolated at the fitted vertex position, to calculate track-pair opening angle in the transverse plane (Fig. 6(a)) and the invariant mass (Fig. 6(b)). Both distributions are obtained from candidates reconstructed in the whole Tracker; the last bin of Fig. 6(b) collects the overflows. The change of slope in the invariant mass distribution is due to candidates reconstructed in the forward Tracker.

The reconstructed conversion pseudo-rapidity (η) and azimuthal angle (ϕ), measured from the direction of the track-pair momentum, are shown in Figs. 7(a), 7(b) respectively, for the whole Tracker. In Fig. 7(c) the ϕ distribution is shown for Pixel barrel ($|z| < 26$ cm and $R < 19$ cm) where the structure due to the Pixel detector cooling pipes is clearly visible. Figure 7(d) finally shows the ϕ distribution of the Inner Silicon barrel ($|z| < 73$cm and $R > 22$cm). The shape of the distribution reflects both the structure of the material as well as the effect of a small number of non working modules. In Fig. 8(a) the radial position of conversions is shown, selecting $|z| <$ 26 cm, i.e. integrating on the very central part of the barrel; the beam pipe, three Pixel layers

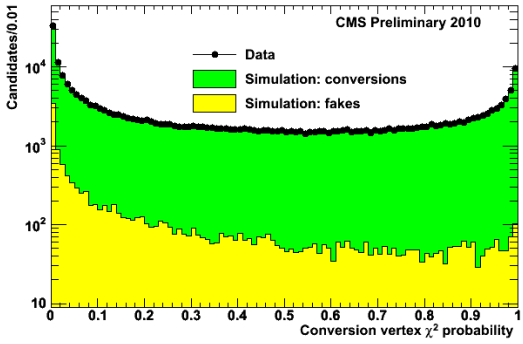

Figure 5: Distribution of the vertex χ^2 probability, with all selection cuts applied.

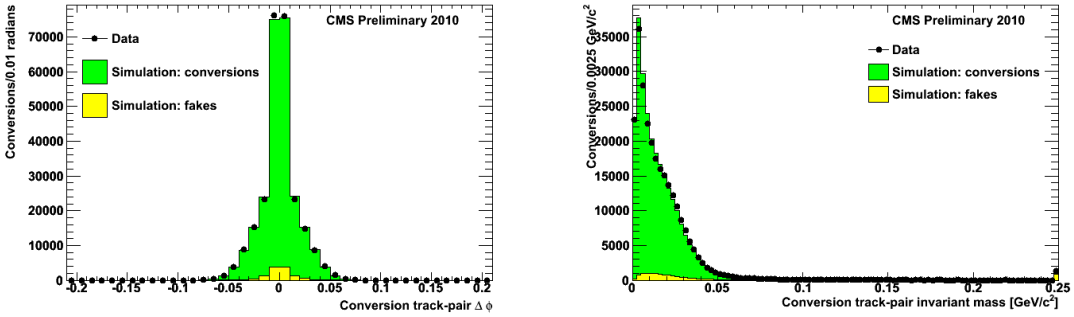

(a) (b)

Figure 6: Electron-positron opening angle in the transverse plane (a) and invariant mass (b). The expected contribution from fakes is also shown.

and the four inner barrel strip layers are clearly seen. In data the vertex position is calculated with respect to the centre of the Pixel barrel detector to account for the overall shift between the Tracker and the nominal reference frame as measured by the alignment group ($x = -0.147\,\text{cm}$, $y = -0.378\,\text{cm}$, $z = -0.485\,\text{cm}$). In Fig. 8(b) the longitudinal coordinate is plotted, selecting the Pixel detector by requiring $3.5\,\text{cm} < R < 19\,\text{cm}$. In general the distributions are very well described by the simulation, with only limited localized discrepancies.

Conversion vertices are reconstructed with an excellent precision: the angular resolution is about 1mrad while the radial resolution varies from about 0.2 cm to about 0.5 cm, primarily as a function of pseudo-rapidity. In Fig. 9 the position of conversion vertices reconstructed in data is shown in the (x, y) plane: in Fig. 9(a) the structure at the very centre is the Pixel detector, surrounded by the shell and rails supporting the Pixel detector, four layers of the Inner Tracker and the first layer of the Outer Tracker. When restricting the (x, y) view to $\pm 12\,\text{cm}$, Fig. 9(c), the beam pipe is clearly visible, off-centered with respect to the Pixel detector. More details on the features visible on the "radiographies" are given in Sec. 6.

The (z, R) view of conversion vertices reconstructed in data is finally shown in Fig. 10; the less populated areas around $|\eta| \sim 1.2$, also present in simulation, correspond to transition regions between the Tracker barrel and endcap sub-components for which the additional track seeding iterations described in Sec. 3 have not been optimized and the conversion reconstruction efficiency is smaller.

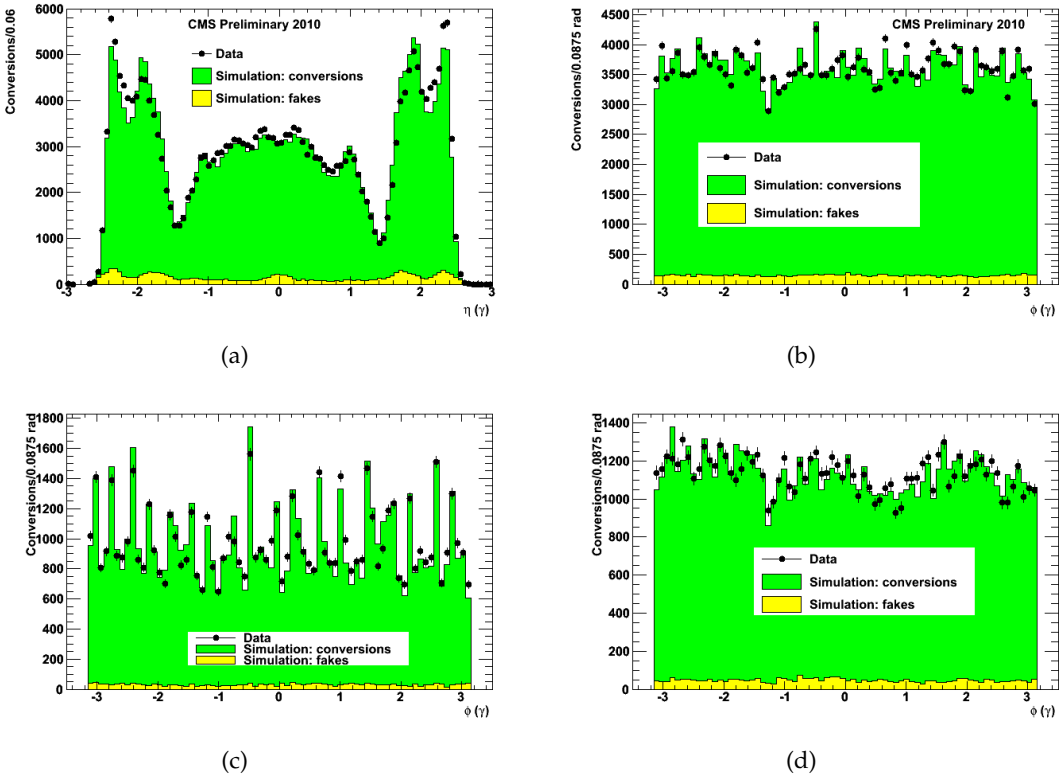

Figure 7: Pseudo-rapidity distribution (a) and ϕ distribution (b) for all conversion candidates, as reconstructed from the track-pair momentum. The ϕ distribution for candidates selected in the Pixel barrel with $|z| < 26\,\text{cm}$ and $R < 19\,\text{cm}$ (c) and in the Inner Strip barrel with $|z| < 73\,\text{cm}$ and $R > 22\,\text{cm}$ (d). The contribution expected from fakes is shown in all plots.

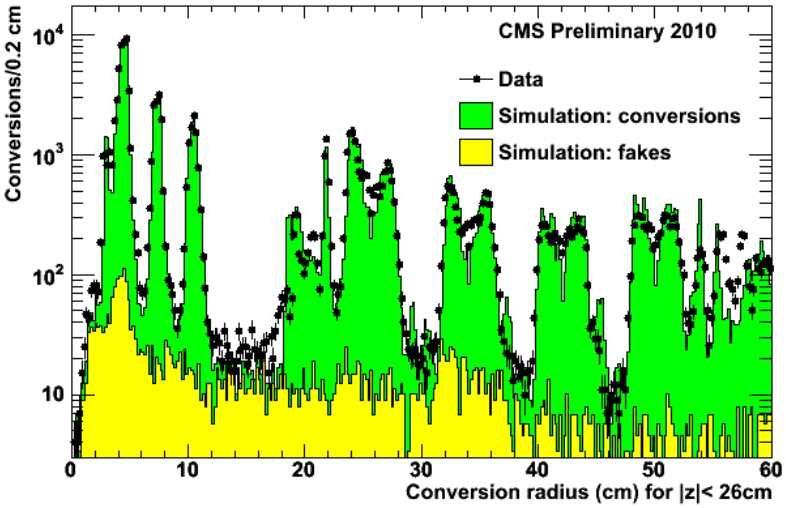

(a)

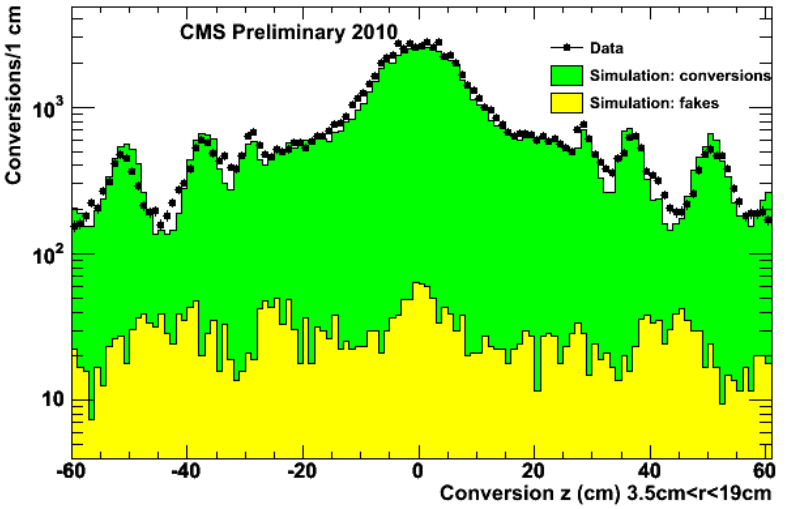

(b)

Figure 8: Conversion vertices: distributions of the radial position for $|z| < 26\,\text{cm}$, i.e. the central portion of the Tracker barrel (a), and longitudinal position for $3.5\,\text{cm} < R < 19\,\text{cm}$, i.e. Pixel Detector, (b). In data the radius is calculated with respect to the centre of the Pixel detector.

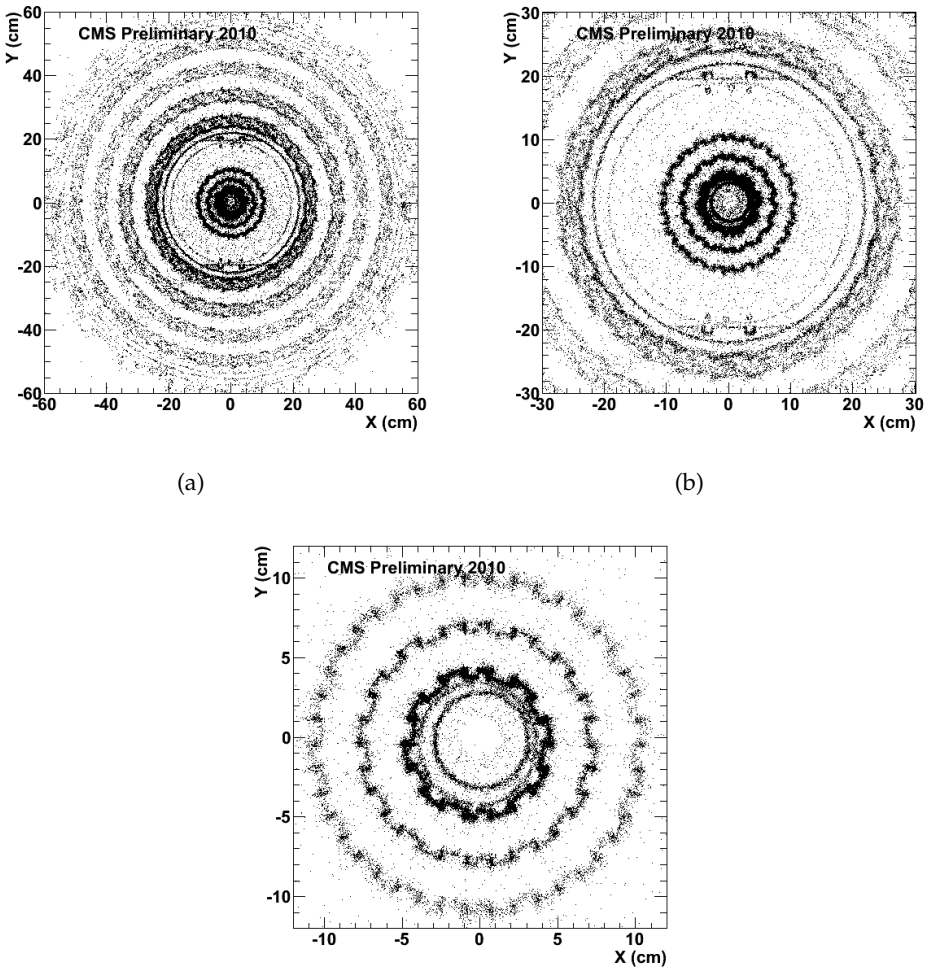

(a) (b)

(c)

Figure 9: Conversion vertices in data in the (x, y) plane for $|z| < 26\,\text{cm}$; zoom increases from (a) to (c).

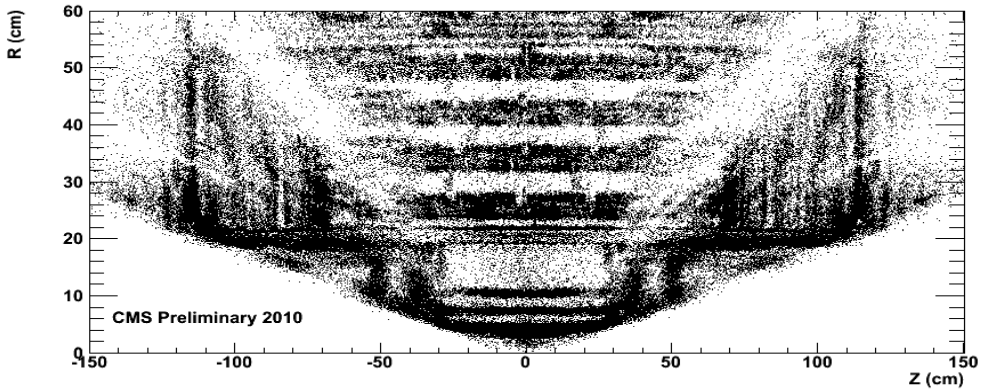

Figure 10: Conversion vertices in data the (z, R) plane.

5 Nuclear Interaction Reconstruction

The overall material distribution of the Silicon Tracker varies between $0.1 - 0.5\,\lambda_{\mathrm{I}}$, where λ_{I} is a characteristic nuclear interaction length [5]. Simulations show that typically 5% of the charged pions with $p_T \approx 5\,\mathrm{GeV}/c$ interact in the Tracker. Thus a large number of nuclear interactions is expected in each event.

Nuclear interactions can be reconstructed when two or more charged tracks participate to the vertex. One of these tracks can be the impinging particle itself, since nuclear interactions may result from either charged or neutral hadrons. The resulting invariant mass distribution of the secondary system extends well above few hundreds of MeV, so that the secondary tracks have a substantial opening angle. This results in a very good vertex spatial resolution, of the order of about $100\,\mu$m, for both the radial and the transverse coordinates of the reconstructed nuclear interaction vertices.

The reconstruction of nuclear interactions is fully based on the Tracker information and it is described in [2]. Two significant upgrades have been implemented:

- the additional tracking steps described in 3 are used with a beneficial impact on the reconstruction efficiency;
- the sizeable statistics accumulated at $\sqrt{s} = 7\,\mathrm{TeV}$ allows some cuts to be tightened to improve the purity of the sample: at least two secondary tracks are required, regardless to the presence of the primary track; the total invariant mass of the outgoing tracks M_{out} is required to exceed $0.6\,\mathrm{GeV}/c^2$ and the total transverse momentum to be greater than $0.5\,\mathrm{GeV}/c$.

The total number of nuclear interaction candidates reconstructed in data is about 570 thousand. The contribution from fake nuclear interactions is estimated from simulated data; true nuclear interactions are identified by accessing the simulation truth. Reconstructed nulear interactions in simulated data are matched to true nuclear interactions by using the same association criteria as described in Sec. 4.

The distributions of reconstructed kinematic quantities related to the nuclear interactions are shown in Fig. 11; the momentum of the incoming track $P_{T,\mathrm{in}}$ when present (Fig. 11 (a)) and the invariant mass, M_{out}, of the secondary tracks (Fig. 11 (b)). The overall agreement between the data and the simulation points toward a reasonable description of the nuclear interaction cross section and kinematics in the simulation.

The η distribution of the nuclear interactions is shown in Fig. 12 (a). The longitudinal coordinate z of the nuclear interactions distribution in Pixel detector is shown in Fig. 12 (b). The Pixel detector region was selected by applying a lower cut in the transverse coordinate, $R > 3.3\,\mathrm{cm}$, which excludes the beam pipe contribution, and an upper cut, $R < 19\,\mathrm{cm}$, which removes the Silicon Strip Tracker contribution. The transverse coordinate R of nuclear interactions in the barrel part of the detector is shown on the Fig. 13 selected by requiring $|z| < 26\,\mathrm{cm}$. It can be seen that very fine details of the material in the Tracker are resolved with this technique. For the data, the vertex position, and consequently the radius and the z coordinate, are computed with respect to the average centre of the Pixel barrel detector as in Section 4. An overall good agreement between data and simulation is observed, while local differences point to regions where there might be a discrepancy between the simulated and the real material distribution.

For example the nuclear interactions distributions are sensitive to the shift of the global structures under study with respect to the nominal origin of the CMS reference system. In Fig. 14 the radial distribution of the nuclear interactions in the region of the beam pipe and the three

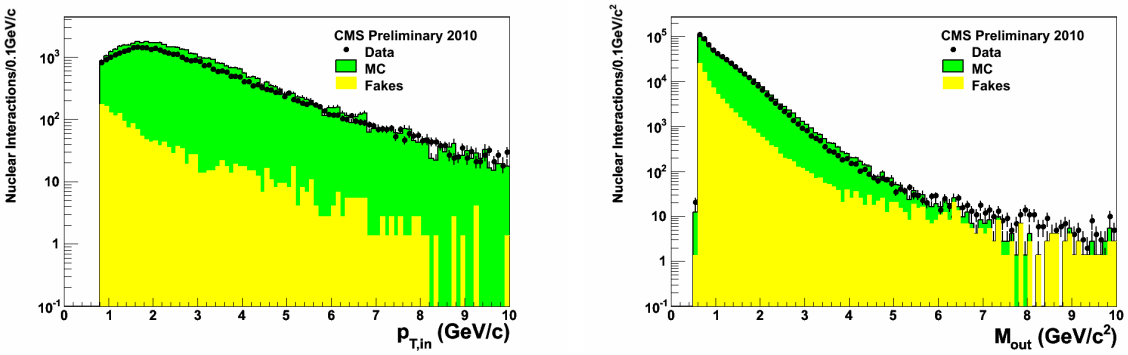

(a) (b)

Figure 11: Momentum distribution of the primary track (a) and invariant mass distribution of secondary tracks (b). The simulation is normalised to the total number of nuclear interactions reconstructed in data in all the Tracker.

Pixel barrel layers is shown. In Fig. 14 (a) the transverse radius is computed with respect to the actual centre of the beam pipe. The beam pipe centre was fitted using the distributions of nuclear interactions in x and y coordinates in slices of 5 cm between $z = -30$ cm and $z = 30$ cm. Those distributions confirm that the beam pipe is circular with a typical thickness of 500 μm, but shifted in x and y and tilted with respect to z axis. The position of the beam pipe centre was parametrized by $x_0 = (0.086\,\text{cm}) - 0.0007 \cdot z$ and $y_0 = (-0.197\,\text{cm}) + 0.0007 \cdot z$ where x_0, y_0 and z are expressed in cm. Thanks to this correction, an excellent agreement between data and simulation is achieved on the beam pipe peak, as shown in Fig. 14 (a). In Fig. 14 (b) the transverse radius is computed with respect to the actual centre of the Pixel barrel and a better agreement is achieved in the peaks corresponding to the Pixel barrel layers.

The high statistics and the sub-millimeter resolution of the nuclear interactions allow to resolve the position of simple objects with a precision of the order of 10 μm. The beam pipe is consequently a good reference for validating our understanding of the nuclear interactions.

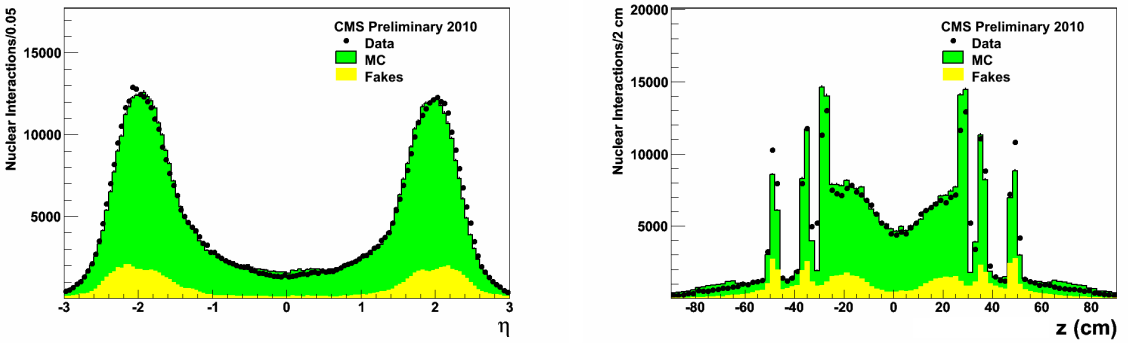

(a) (b)

Figure 12: Distribution of pseudo-rapidity (a) and z coordinate restricted to the Pixel barrel (3.3 cm $< R <$ 19 cm) (b), for reconstructed nuclear interaction vertices in data and simulation. In data the coordinates are computed with respect to the actual average Pixel barrel centre. The contribution from fakes is also shown.

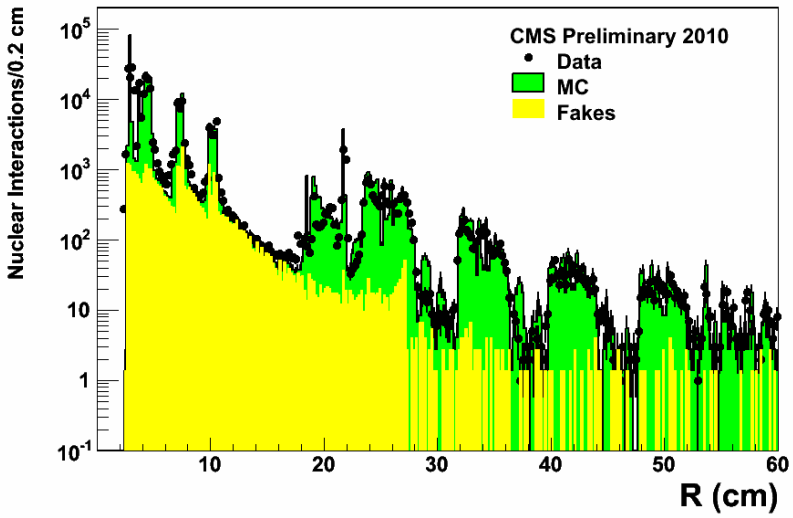

Figure 13: Distribution of the transverse radius of the reconstructed nuclear interaction vertices for data and simulation. In data the coordinates are computed with respect to the actual average Pixel barrel centre.

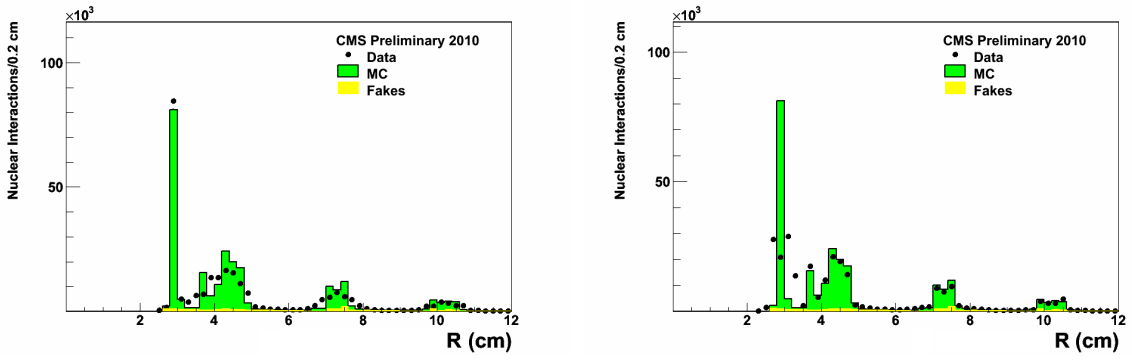

(a) (b)

Figure 14: Distribution of the transverse radius for the nuclear interaction vertices: in data the coordinates are computed with respect to the beam pipe centre in (a) and with respect to the actual centre of the Pixel barrel in (b).

6 Material plots from photon conversions and nuclear interactions

The counting experiments of photon conversion and nuclear interaction in a volume depend on the amount of material in that volume, as well as on the reconstruction efficiency and on the impinging photons or hadrons flux. In particular, assuming a negligible background from fakes, the number of reconstructed photon conversion N_{conv} in a given volume is

$$N_{\text{conv}} \propto \varepsilon_{\text{conv}} \cdot \langle \frac{P}{X_0} \rangle \cdot f_{\text{geom}}, \tag{1}$$

where $\varepsilon_{\text{conv}}$ is the reconstruction efficiency and $\langle P/X_0 \rangle$ is the average conversion probability ($P \sim 7/9$). A similar formula can be written for nuclear interactions:

$$N_{\text{n.i.}} \propto \varepsilon_{\text{n.i.}} \cdot \langle \frac{1}{\lambda_I} \rangle \cdot f_{\text{geom}}. \tag{2}$$

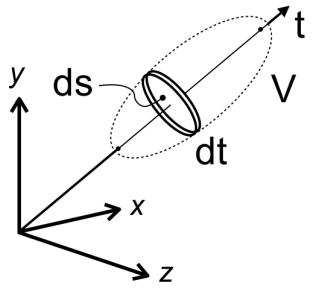

Figure 15: Pictorial representation of the derivation of the geometrical factor for the volume V.

As sketched in Fig. 15, the geometrical correction factor f_{geom} for a volume V results from the integration

$$f_{\text{geom}}^{\text{V}} = \int_V \Phi(t) \cdot ds dt, \tag{3}$$

where t runs along the photon or hadrons arrival direction (assumed to be uniform over the volume), and $\Phi(t)$ is the flux normalised to the total number of photons or hadrons, respectively. The correction factors method follows the approach used in reference [12]. The photon or hadron flux is approximately assumed to be flat in η, to scale as $1/r^2$ (r being the radius in a spherical coordinate system), and to originate from $(0, 0, 0)$. Within these assumptions the flux is proportional to $1/(r^2 \sin^2 \theta)$ and can be easily integrated (analytically or numerically) over the volume under observation.

The plots in this section report the raw numbers of reconstructed photon conversions, N_{conv}, and of reconstructed nuclear interactions, $N_{\text{n.i.}}$, counted in a given volume and corrected by using the following expressions:

$$\frac{1}{N_{\text{events}}} \cdot \frac{N_{\text{conv}} - N_{\text{conv}}^{\text{fakes}}}{\varepsilon_{\text{conv}} \cdot f_{\text{geom}}}, \tag{4}$$

$$\frac{1}{N_{\text{events}}} \cdot \frac{N_{\text{n.i.}} - N_{\text{n.i.}}^{\text{fakes}}}{\varepsilon_{\text{n.i.}} \cdot f_{\text{geom}}}. \tag{5}$$

The efficiencies $\varepsilon_{\text{conv}}$ and $\varepsilon_{\text{n.i.}}$ and the number of fakes for photon conversions, $N_{\text{conv}}^{\text{fakes}}$, and nuclear interactions, $N_{\text{n.i.}}^{\text{fakes}}$, are estimated from simulation; N_{events} is the number of analysed events.

As a consequence of the definition of the geometrical factor, computed appropriately in each plot bin, the expression (4) represents a quantity proportional to the photon conversion probability, $\langle P/X_0 \rangle$, averaged in the counting volume, multiplied to the number of primary photons per event, N_γ. Similarly, the expression (5) represents a quantity proportional to the nuclear interaction probability, $\langle 1/\lambda_I \rangle$, averaged in the counting volume, multiplied to the number of primary hadrons per event, N_{had}.

The present statistics allow only the Pixel barrel (PXL) and the Inner Tracker barrel (TIB) to be studied. The regions represented in the following plots are defined by appropriate fiducial cuts on the radius and the z coordinate of the reconstructed vertices, as specified below. In the following, data and simulation are normalised to the same number of candidates of photon conversions or nuclear interactions within the volume under study, so that relative information regarding the distribution of material inside the region under study can be derived. Since the plots are limited to the barrel region, for the present results the efficiency is assumed to change only as a function of the radius.

6.1 Material plots versus radius

The raw reconstructed radial distributions of photon conversion and nuclear interaction counting of Fig. 8(a) and Fig. 13 are treated with the procedure outlined above. The resulting material distributions for photon conversions and nuclear interactions are shown in Fig. 16. The plots have been produced for a fiducial volume designed to contain the envelope of the Pixel detector barrel and the Inner Tracker barrel; in particular $|z| < 26.0\,\mathrm{cm}$ for $2.0\,\mathrm{cm} < R < 20.0\,\mathrm{cm}$ and $|z| < 66.0\,\mathrm{cm}$ for $20.0\,\mathrm{cm} < R < 65.0\,\mathrm{cm}$. Due to lack of statistic at large radii, the fiducial volume in case of nuclear interaction ends at $R < 61.0\,\mathrm{cm}$. The beam pipe shape is not perfectly reproduced in Fig. 16 (b) since the nuclear interaction radius is calculated with respect to the Pixel barrel detector centre (see Fig. 14).

The plots in Fig. 16 clearly demonstrate a very good agreement between data and simulation for both photon conversions and nuclear interactions, showing that the description of the Tracker material in the simulation is well under control. More quantitatively, the ratio between the number of candidates in data and simulation (after fakes subtraction) can be directly related to material discrepancies between the real and simulated Tracker. This quantity is shown in Fig. 17 for several radial bins, each containing one substructure, for both photon conversion and nuclear interaction reconstruction in the same region used for the plots in Fig. 16. Pixel layer 1 and beam pipe are merged in a single bin because the respective contributions cannot be easily separated in case of photon conversions. Since the total number of candidates in simulation is normalised to data in the region under study, Fig. 17 represents a quantitative comparison of the shapes in the radial material distributions between data and simulation. No attempt is presently made to evaluate systematic uncertainties, and the error bars in Fig. 17 reflect only statistical errors. Overall the observed relative agreement is of the order of $\sim 10\%$, except a localized larger discrepancy in the "support" region between TIB and Tracker Outer Barrel (TOB).

6.2 Material maps

The spatial information of the reconstructed vertices can be used to build detailed maps of the Tracker material in regions of interest. In Figure 18 the x-y cross sections of the material distribution for the Pixel barrel and the Inner Tracker barrel region are shown, as obtained for the simulation truth, simulation reconstructed, and data. The fiducial cut on which the distributions are built is $|z| < 26.0\,\mathrm{cm}$ for $1.0\,\mathrm{cm} < R < 20.0\,\mathrm{cm}$ and $|z| < 66.0\,\mathrm{cm}$ for $20.0\,\mathrm{cm} < R < 65.0\,\mathrm{cm}$; the normalisation procedure for geometrical factors and efficiency described at

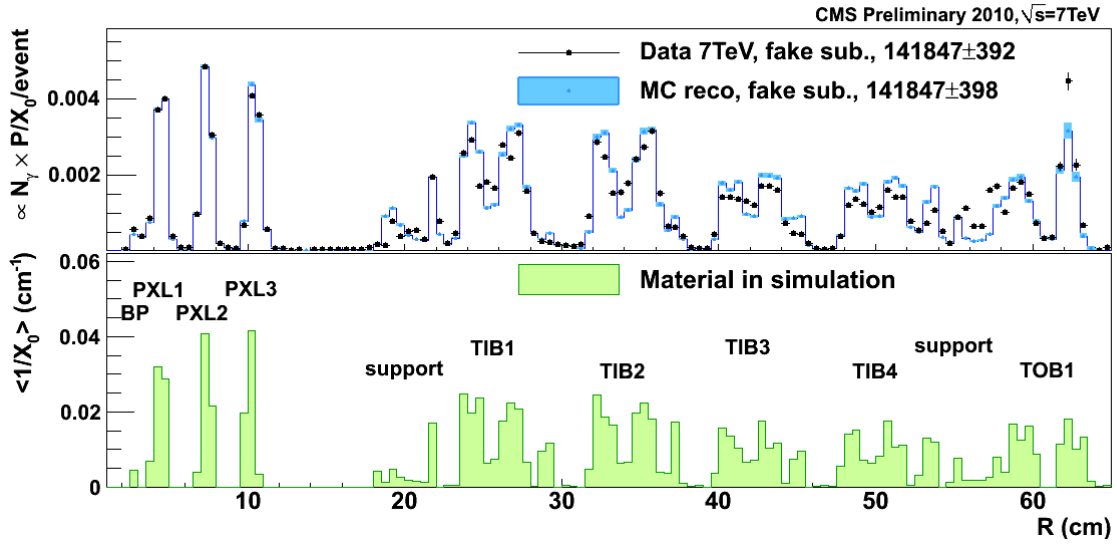

(a)

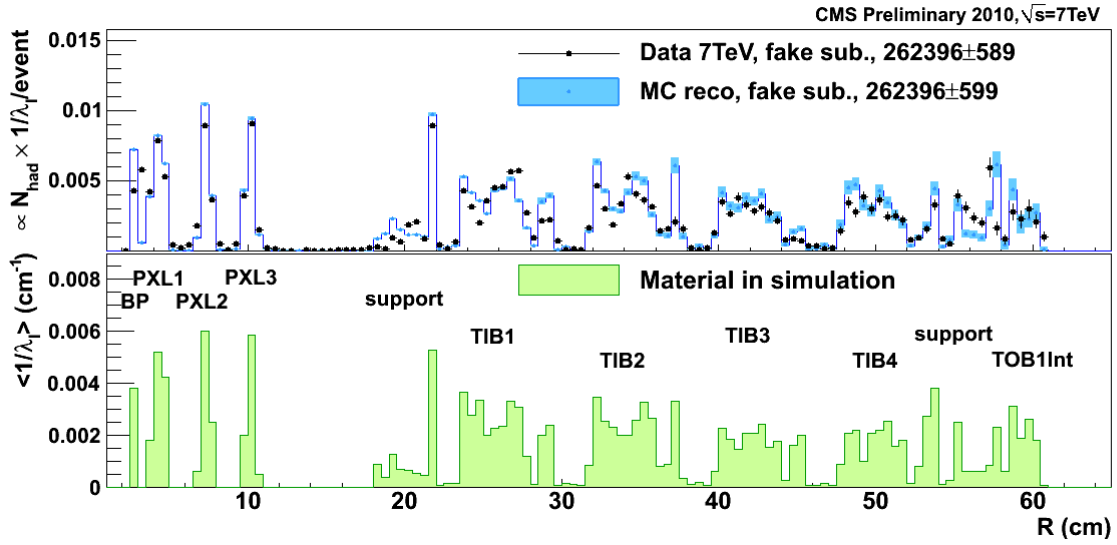

(b)

Figure 16: Material distribution versus the radius estimated from reconstructed photon conversions (a) and nuclear interactions (b). The radius is calculated with respect to the Pixel barrel detector centre. As a comparison, the histogram in the bottom panel represents the material distribution in the simulation in average X_0^{-1} per bin (a), and in average λ_I^{-1} per bin (b). In both plots the radius bin width is 0.5 cm.

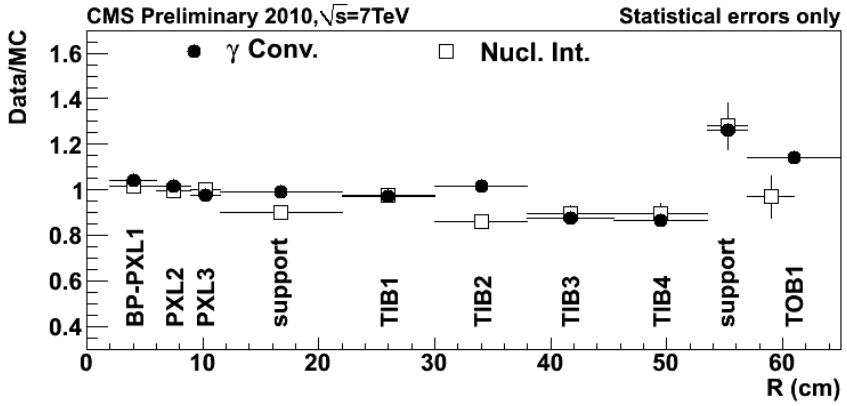

Figure 17: Ratio of number of candidates (after fake subtraction) in data over simulation for photon conversion reconstruction (•) and nuclear interaction reconstruction (□) for radius bins embracing the major Pixel barrel or Inner Tracker substructures, statistical errors only are shown.

the beginning of the present section is applied. In Fig. 19 a zoom into the first layer of the Inner Strip barrel and the Pixel barrel region is shown.

The comparison of data based and simulation based maps clearly show that the CMS Tracker simulation is very realistic, but there are still some difference between the actual Tracker and what has been implemented in the simulation. These differences are due to complex structures that have been simulated with simplified volumes nominally equivalent in mass and chemical composition; the Pixel detector support rails visible in the region comprised between $-10.0\,\text{cm}$ and $10.0\,\text{cm}$ in x for $y \sim \pm 19.0\,\text{cm}$ of Fig. 19 (e) and (f) are an example. Other differences are due to structures that in the simulation have a different size or are omitted. The Pixel barrel shield, the faint circular structure with a radius of $\sim 20.0\,\text{cm}$ visible in Fig. 19 (e) and (f), in the simulation has a radius $\sim 1\,\text{cm}$ smaller. The two pairs of stiffening hollow carbon fiber rods connecting the Pixel barrel flanges, which are also visible in Fig. 19 (e) and (f), close to the Pixel detector rails, are missing in the simulation. The material maps from data also show that the beam pipe is off-centered with respect to the Pixel barrel.

In Figs. 20 and 21, z-R maps of the Pixel and Inner Tracker regions are shown for photon conversions and nuclear interactions, respectively. The region on which the distributions are built is defined by the cuts $|z| < 55.0\,\text{cm}$ and $1.0\,\text{cm} < R < 54.0\,\text{cm}$; the procedure described at the beginning of the present section is applied.

The nuclear interaction z-R view of Fig. 21(c) in the region $25.0\,\text{cm} < |z| < 35.0\,\text{cm}$ allows the complicated configuration of the Pixel barrel end-flange to be appreciated, with cables and cooling pipes clearly visible. It is normal to represent complicated structures in the simulation with simplified volumes. These details can be seen in the x-y maps of Fig. 22 obtained with nuclear interaction samples belonging to the z slices where the cooling pipes are located, i.e. $-33.0\,\text{cm} < z < -29.0\,\text{cm}$ and $29.0\,\text{cm} < z < 33.0\,\text{cm}$, conveniently overlapped. In particular, as visible in Fig. 22 (a) and (b), the simulation contains volumes placed within the above mentioned z slices, not realistic in shape, but filled with material mixtures to result equivalent in mass and chemical composition to the real materials. The density of these volumes varies as a function of the radius to take into account that services, pipes and cables become more sparse as they run away from the z-axis (Fig. 22 (c)).

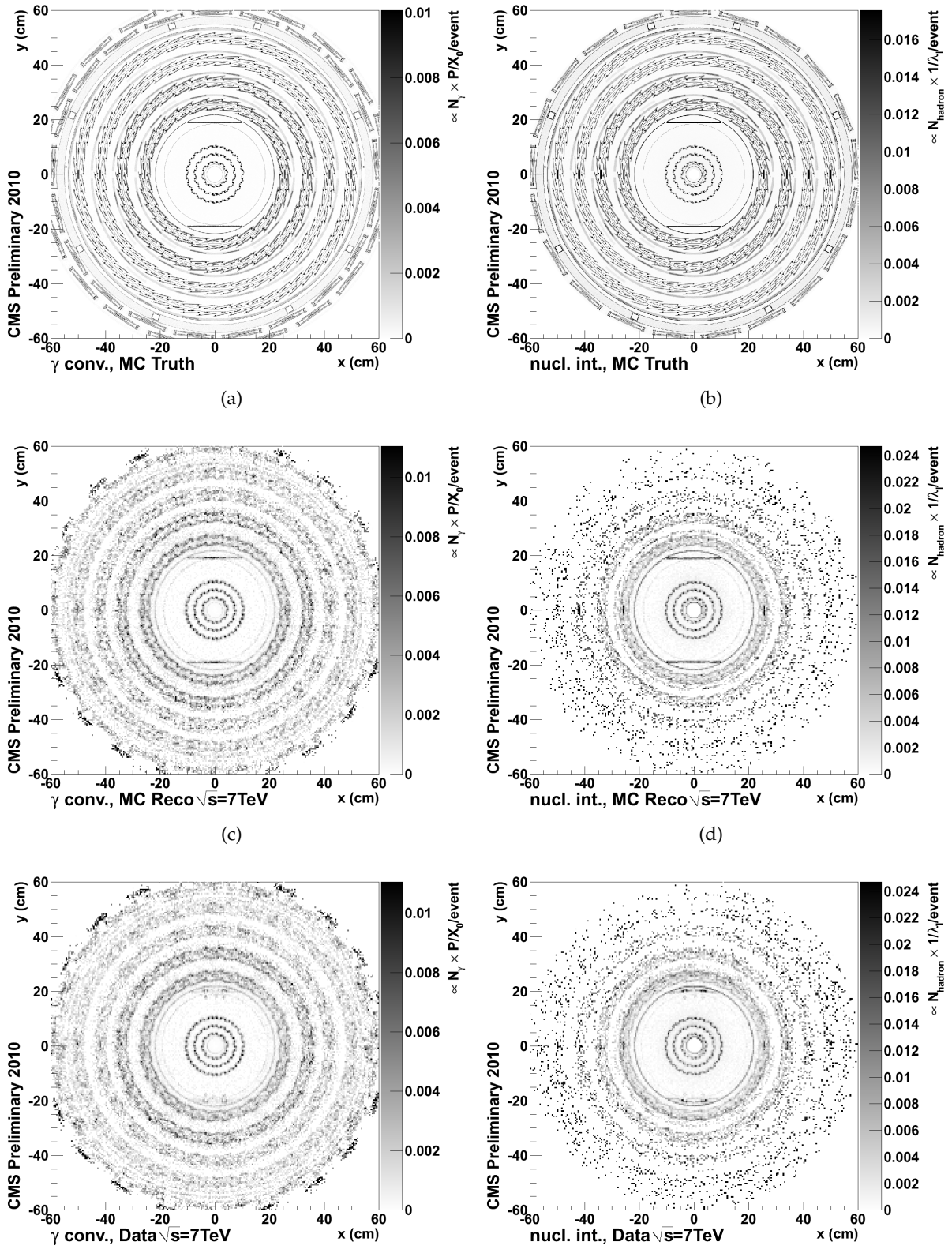

(a) (b)

(c) (d)

(e) (f)

Figure 18: Maps of the x-y cross section of the material distribution for photon conversions (left column) and nuclear interactions (right column), Pixel barrel and TIB region: (a), (b) show the simulation truth (x-y bin size $0.1 \times 0.1\,\mathrm{cm}^2$); (c), (d) show the simulation reconstructed (x-y bin size $0.5 \times 0.5\,\mathrm{cm}^2$); (e), (f) are the reconstructed distributions in data (x-y bin size $0.5 \times 0.5\,\mathrm{cm}^2$).

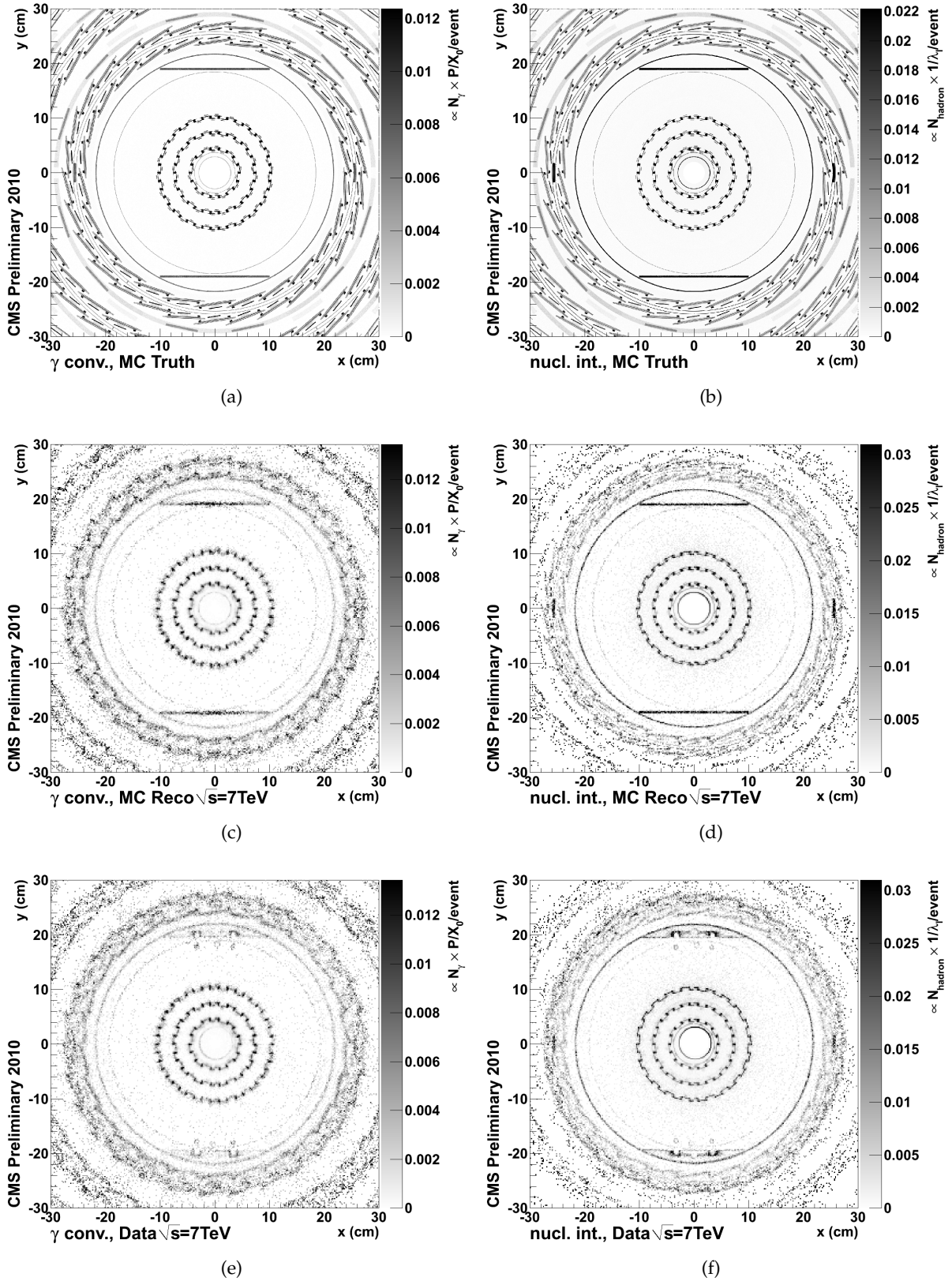

Figure 19: Zoom in the PXL barrel region of the plots of Fig. 18. Same conventions apply. The x-y bin size is $0.5 \times 0.5\,\mathrm{mm}^2$ for (a), (b), and $0.2 \times 0.2\,\mathrm{cm}^2$ for (c), (d), (e), (f).

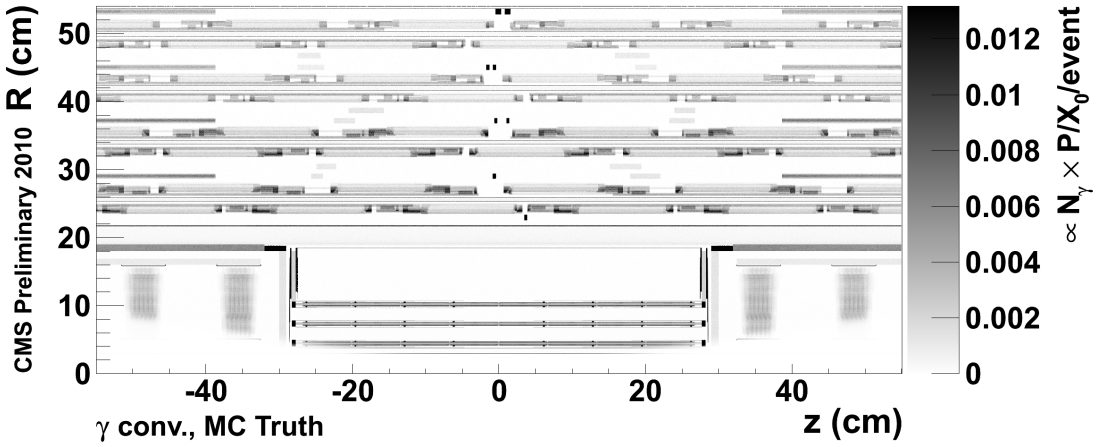

(a)

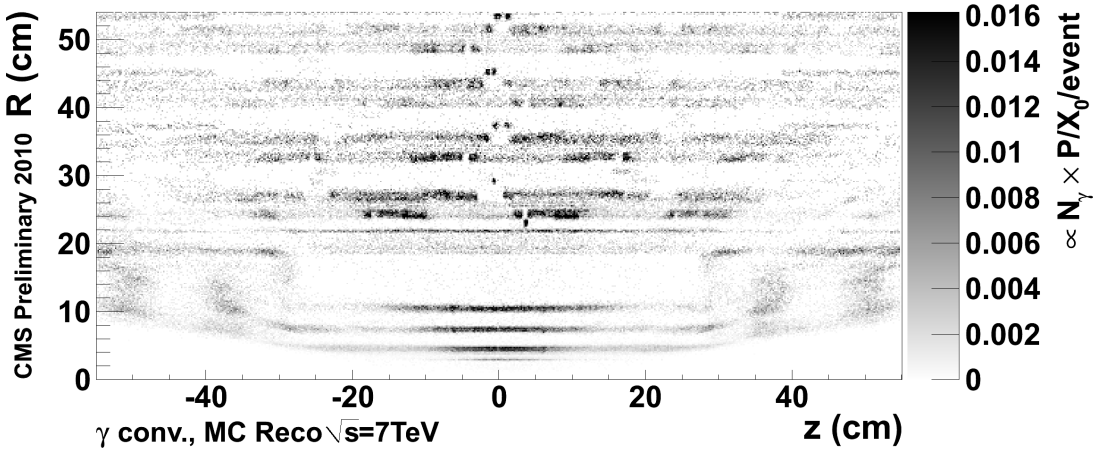

(b)

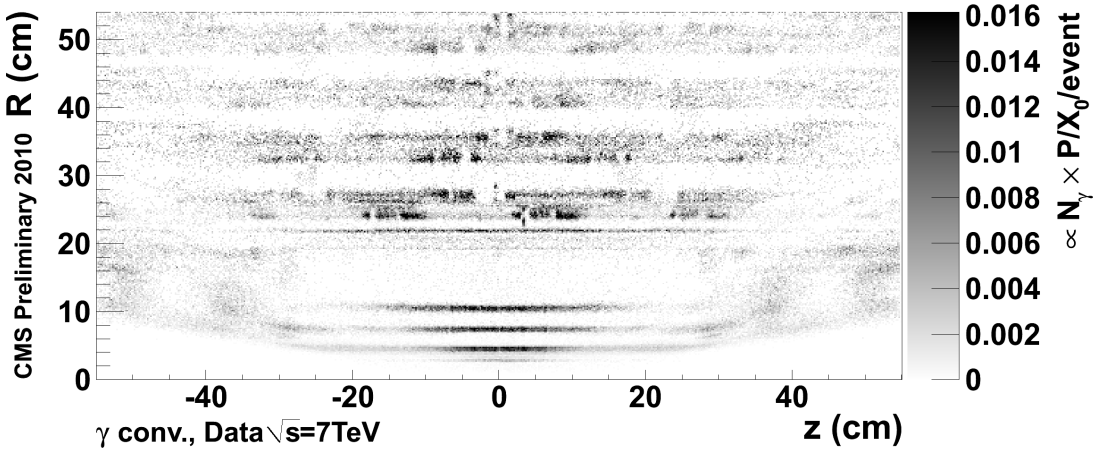

(c)

Figure 20: Maps of the z-R cross section of the material distribution for photon conversions: simulation truth (a), simulation reconstructed (b), and data (c). The z-R bin size is $0.5 \times 0.5\,\mathrm{mm}^2$ for (a), and $0.2 \times 0.2\,\mathrm{cm}^2$ for (b), (c).

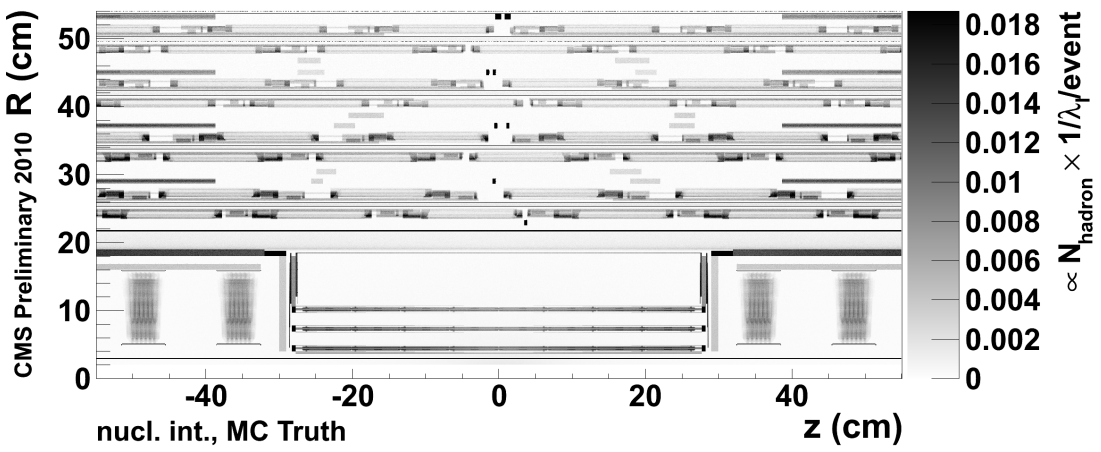

(a)

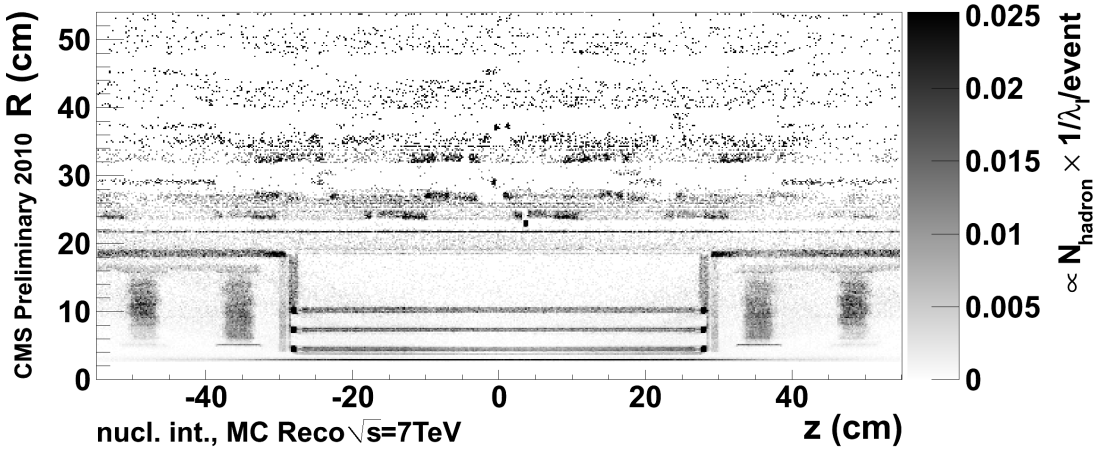

(b)

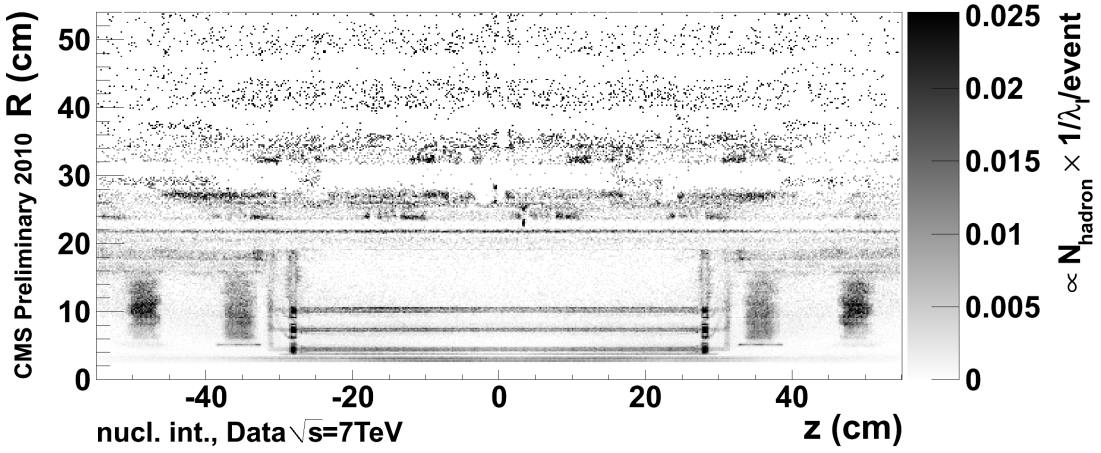

(c)

Figure 21: Maps of the z-R cross section of the material distribution for nuclear interactions: simulation truth (a), simulation reconstructed (b), and data (c). The z-R bin size is $0.5 \times 0.5\,\mathrm{mm}^2$ for (a), and $0.2 \times 0.2\,\mathrm{cm}^2$ for (b), (c).

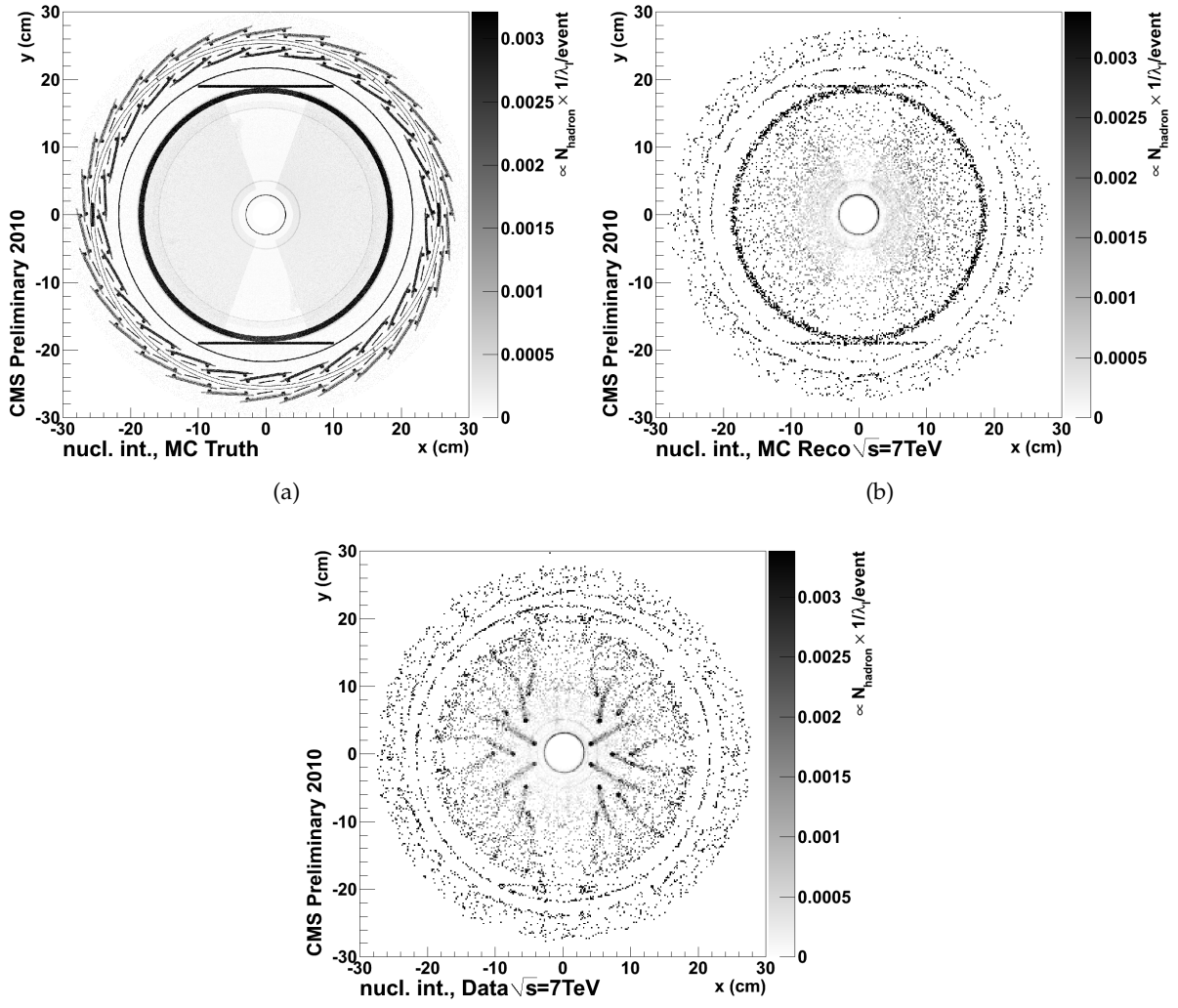

(a) (b)

(c)

Figure 22: Maps of the x-y cross section of the material distribution for nuclear interactions for $-33.0\,\text{cm} < z < -29.0\,\text{cm}$ and $29.0\,\text{cm} < z < 33.0\,\text{cm}$: simulation truth (a), simulation reconstructed (b), and data (c). The x-y bin size is $0.5 \times 0.5\,\text{mm}^2$ for (a), and $0.2 \times 0.2\,\text{cm}^2$ for (b), (c).

6.3 Local views

In the previous plots, reconstructed conversion and nuclear interaction vertices have been displayed in global coordinates views (x-y, R, z-R). Nevertheless the CMS Tracker design is largely modular, with a large number of elementary structures, like silicon modules, that exist in few flavours but in very large number of identical items. This modularity is translated in the GEANT4 simulation where an identical substructure, the module logical volume, for example, is replicated where needed.

This modularity can be exploited to make more efficient use of the available statistics for a detailed investigation of the material of these repeating objects. To do this, the global coordinates of a 3D point (i.e. the nuclear interaction or conversion vertex) are translated in the local frame of the nearest module. In particular, to a given position of a global point $(x_{\text{global}}, y_{\text{global}}, z_{\text{global}})$ in the CMS reference frame (as provided by the reconstruction) is associated the position in the local frame of the nearest measurement surface $(x_{\text{local}}, y_{\text{local}}, z_{\text{local}})$. For a barrel strip module, the coordinate y_{local} runs parallel to the strips with the positive direction pointing away from the readout chips; the coordinate z_{local} is normal to the silicon surface pointing outward with respect to the strip side; the coordinate x_{local} runs along the silicon surface orthogonal to the strips, with the positive direction oriented accordingly to a right-handed reference system.

Presently, only modules have been studied. The procedure is affected by mis-alignment effects that have not been compensated for the present studies.

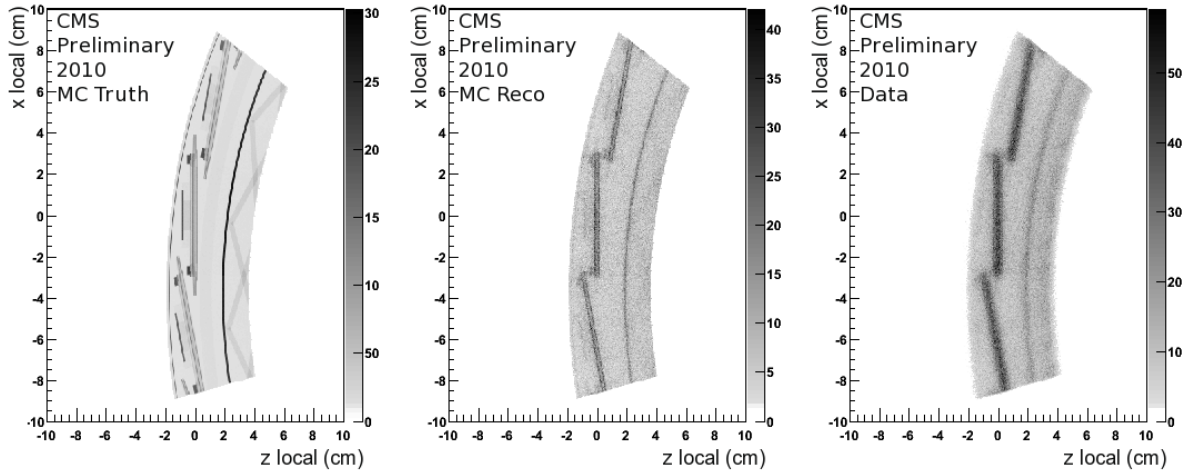

(a) (b) (c)

Figure 23: Nuclear interaction local view of the x_{local} vs. z_{local} projection related to the Inner Tracker Layer 1, internal part: (a) simulation truth; (b) simulation reconstructed; (c) data.

As an example of this technique, the local transverse view, x_{local} vs. z_{local} with respect to the Rϕ module, of the Inner Strip Tracker Layer 1, internal, is shown in Fig. 23 for nuclear interaction vertices. Each plot features the single module local view replicated three times, with the appropriate relative geometry, to mock-up a portion of the structure. The data based plot of Fig. 23 (c) shows the structures expected in the simulation but affected by the smearing due to misalignment and unavoidable irregularities of the passive structures.

7 Multiple Scattering method

Multiple scattering is an important component of the overall Tracker momentum resolution function: it is the dominant component for tracks with P_T up to well over 10 GeV/c, and remains a substantial component even at P_T of 100 GeV/c.

The effect of multiple scattering on the reconstructed track trajectories can be exploited to probe the amount of material in the volume where particles travel. The method is based on the standard CMS track reconstruction algorithm. On each detection surface containing a measurement this algorithm provides the five estimated track parameters together with their uncertainties, which are represented by a five by five covariance matrix. The five track parameter and the associated covariance matrix will be referred to as the track state on the considered detection plane. In order to estimate the amount of material existing between two given detection planes, the track state on the inner plane (also called starting plane) is extrapolated to the outer plane (also called destination plane) under a certain assumption for the amount of material, which is the quantity that must be measured. The uncertainty of the extrapolated track state on the outer plane is determined by the multiple scattering that the particle experiences in traversing the assumed amount of material between the two planes and by the uncertainty of the state on the inner plane. For low momentum tracks the former contribution is expected to be dominant over the latter one because the uncertainty on the measurements is by far smaller than the uncertainty caused by multiple scattering. Therefore the uncertainty of the extrapolated track state on the outer plane carries the information on the estimated effect of the amount of material assumed at track reconstruction level.

On the other hand, on a statistical basis, the residual between the central value of the extrapolated track state and the measurement on the outer plane carries the information on the actual multiple scattering experienced by the particle as it traveled through the material. The central value of the extrapolated track state is mainly determined by the central value of the state on the starting plane. Uncertainties in the knowledge of the magnetic field, positions of the detectors and energy loss (determined by the amount of material) are expected to have a negligible effect on the width of the residual distribution in the case of low momentum track. In addition it must be assumed that the uncertainty on the measurement is either negligible compared to the typical residual or is known without bias, in which case it must be subtracted out on a statistical basis. The assumption of negligible uncertainty on the measured crossing point again holds with very good approximation in the case of low momentum particles and if the residuals are evaluated in the precisely measured coordinate.

The relevant observable that provides a direct comparison between the assumed amount of the material and the actual one is thus the standard deviation of a Gaussian fit to the distribution of the ratio between the residual and the uncertainty on the extrapolated state, where both are intended along the precisely measured coordinate. This quantity will also be called the sigma of the pull distribution related to the considered destination plane and will be indicated by σ_i^{pull}, where i is an index that identifies the destination plane.

The values of σ_i^{pull} must all be equal to unity in case the assumed amount of material coincide with the actual one. Values lower (larger) than unity would indicate an overestimation (underestimation) of the amount of material. This simple interpretation cannot, however, be strictly adopted if the track reconstruction is performed with different material distributions than in the actual detector setup, which is indeed the case. In fact, the material distribution assumed by the CMS track reconstruction algorithm is a simplified one, where all material is concentrated at infinitely thin surfaces corresponding to the position of the detection planes.

This choice is driven by computational time arguments. Note that, to maintain the sensitivity of the method, and avoid unwanted bias, the measurement on the destination plane and all the following measurements are not used in the computation of the track state on the starting plane. For this study the standard track reconstruction with its simplified material distribution was run on both simulation and data. While simulated tracks experience the material present in the simulated setup, real tracks experience the material of the real setup. The ratio of the σ_i^{pull} values obtained on simulation and data provides a direct comparison between the amount of material present in the simulated and real setups. A ratio smaller (larger) than unity would indicate that the amount of material in the simulated setup is smaller (larger) that the amount of material in the real setup.

Unlike the methods based on counting conversions and nuclear interactions, this technique does not need the knowledge of any reconstruction efficiency in order to provide an absolute measurement of the amount of material in a tracking detector. Therefore it is not affected by systematics arising from uncertainties on such efficiencies. The method is also expected to suffer little from misalignment and other detector mis-calibrations as long as sufficiently low momentum tracks are employed. Little statistics is sufficient to extract results in the entire tracking detection volume. On the other hand, it should be noted that the method has no or little sensitivity to the actual details of the material distribution between two detection layers.

A fraction of the data and simulation samples detailed in section 2 were analyzed in this study. Good quality tracks produced with transverse (longitudinal) impact parameter with respect to the reconstructed primary vertex smaller than 0.1 cm (1 cm) were selected in different momentum (P) ranges according to their reconstructed pseudo-rapidity (η). The resulting samples (A, B, C, D) are shown in Table 1. This choice is motivated by having tracks with the lowest possible momentum and at the same time capable of reaching the outermost Tracker detection planes.

Sample	A	B	C	D
η range	$0 < \|\eta\| < 0.6$	$0.6 < \|\eta\| < 1.3$	$1.3 < \|\eta\| < 1.7$	$1.7 < \|\eta\| < 2.5$
P range (in GeV/c)	$[1, 1.1]$	$[1.6, 1.8]$	$[2.4, 2.7]$	$[3, 3.3]$

Table 1: Selection of the track momentum ranges in the different pseudo-rapidity ranges considered for this study.

The pull distributions for the TIB, TOB, TID and TEC[1] detection planes are in all cases well fitted by a Gaussian curve. As an example, the pull distributions for the four TIB detection planes obtained with the tracks from sample B (data) are shown in Figs. 24. The σ_i^{pull} values are in general lower than unity. As discussed above, these low values are somehow expected because they could partly be due to the simplified material model adopted in track reconstruction.

The same conclusions do not hold for the distributions related to the pixel detection planes, which seem to be better fitted by the sum of two Gaussian curves with different widths. A possible explanation of this feature could be the presence of zones, within the considered η ranges and, possibly, along the ϕ coordinate, where the level of agreement between the assumed and actual amounts of material are significantly different. A deeper study, requiring a higher granularity, is ongoing to understand the origin of these discrepancies. Given that a simple Gaussian

[1]The Tracker subdetectors are sketched in Fig. 1.

fit is not appropriate for the pull distributions relative to the pixel detection layers, only results related to the silicon strip detection layers are presented in the following.

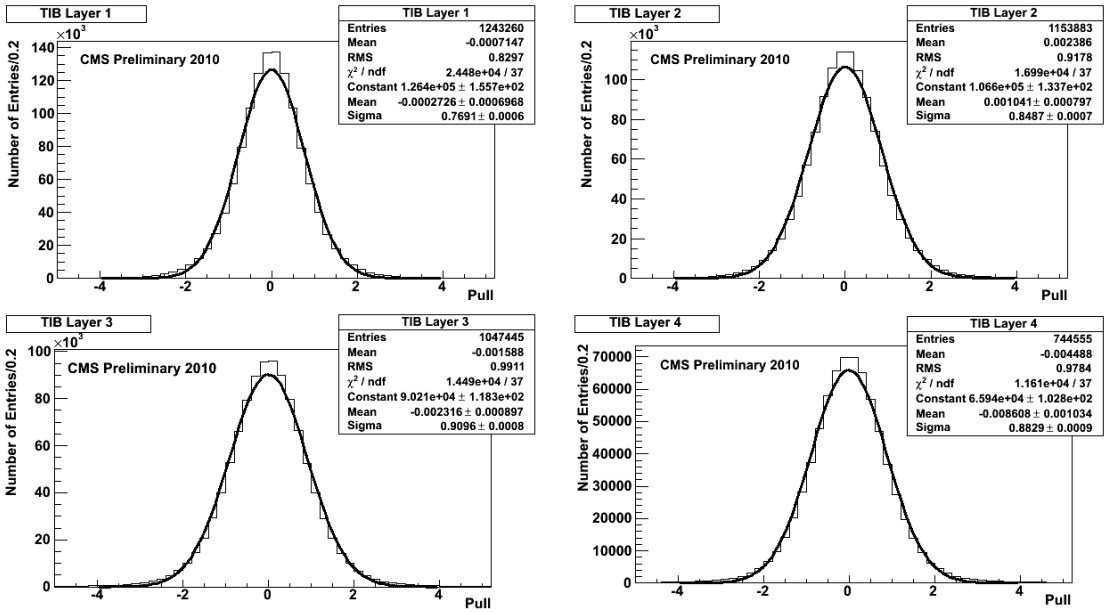

Figure 24: Pull distributions relative to the four TIB detection planes obtained with tracks in sample B (data).

The robustness of the technique with respect to misalignment effects and the sensitivity to differences in the assumed and actual amount of material can be appreciated by computing the σ_i^{pull} values on simulated tracks under different conditions. The following scenarios were considered:

1. a perfectly aligned setup (*ideal*);
2. a misaligned (and mis-calibrated) setup, as expected at the start-up of the experiment [13] (*start-up*); this scenario was implemented under the assumption that only information from survey measurements, the Laser Alignment System and cosmic muon tracks are used to perform a detector alignment;
3. the same misaligned setup, but with an assumed amount of material at the track reconstruction level increased by 20% with respect to the default one, which corresponds to the to the actual material at the detector simulation level;
4. the same misaligned setup, but with an assumed amount of material at the track reconstruction level decreased by 20% with respect to the default one, which corresponds to the to the actual material at the detector simulation level.

Three different ratios of the σ_i^{pull} values obtained in the scenarios listed above are shown in Fig. 25. The uncertainties on these ratios, deriving from the uncertainty on the fitted σ_i^{pull}, are much smaller than the size of the symbols used in the plots. In all cases the results were obtained with sample A. Very similar results are observed for the other barrel η slice (sample B). These results indicate that the method is, for all barrel layers except the first one, indeed sensitive to differences at the level of 20% between assumed and actual amounts of material

and that systematic effects deriving from the misalignment expected at the start-up of the experiment would yield smaller observed discrepancies, of the order of 5%. The small observed value of the σ_i^{pull} ratio between start-up and ideal scenarios for the first barrel layer indicates that differences in these scenarios at alignment level dominate over differences in material at the level of 20%. The results obtained in all endcap layers are similar to those obtained in the nine outer layers of the barrel.

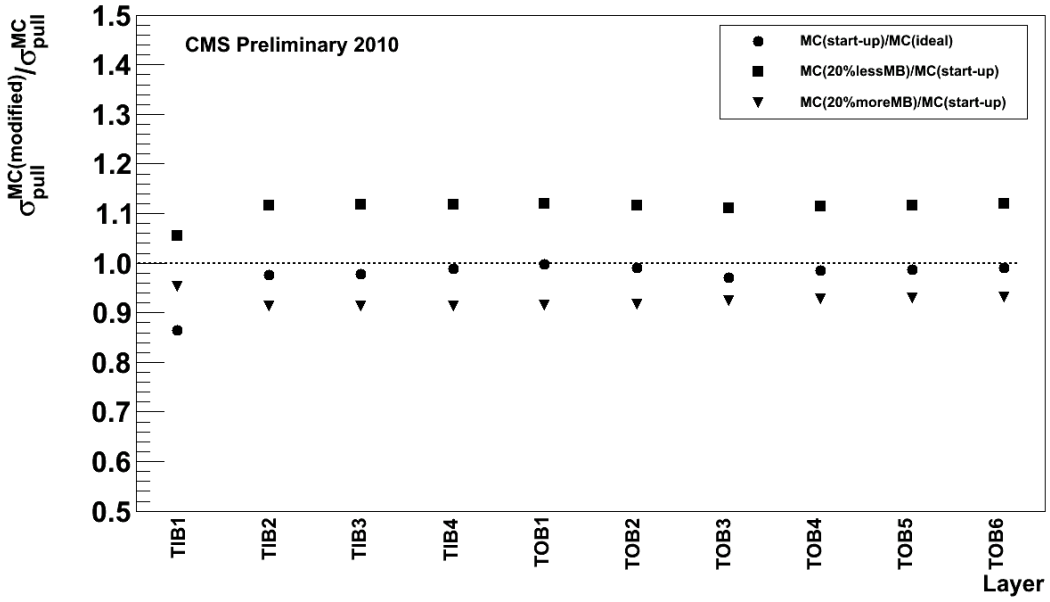

Figure 25: Ratios of the σ_i^{pull} values obtained on the simulated sample A with various assumptions. The circles compare the start-up and ideal scenarios; the triangles and the squares show the effect in the start-up scenario of, respectively, a $+20\%$ and a -20% variation of the material at the reconstruction level. The detection layers on the x-axis are the destination layers.

The ratio of the σ_i^{pull} values obtained on simulation and data for barrel and endcap are shown in Figs. 26 and 27, respectively. Based on the results presented in Fig. 25, a systematic uncertainty of 5% is assigned to the measurements on every detection layer, except for the first barrel layer where a value of 10% is used.

The ratio of the σ_i^{pull} values is generally close to one in all cases. Therefore it can be concluded that the amounts of material in the real and simulated Silicon Strip Tracker detector agree within $\sim 20\%$ in both barrel and endcap regions.

8 Conclusions

Photon conversions and nuclear interactions provide a detailed radiography of the material inside the Inner CMS Tracker up to a radius of about 60 cm from the beam pipe. A good overall agreement, at a level of $\sim 10\%$, is observed between the shapes of the material distributions in the real and simulated Tracker detector, with only a limited number of localized discrepancies.

A new and complementary method that exploits the multiple scattering experienced by low momentum particles indicates that the amounts of material in the real and simulated Tracker detector agree within $\sim 20\%$ in both barrel and endcap regions.

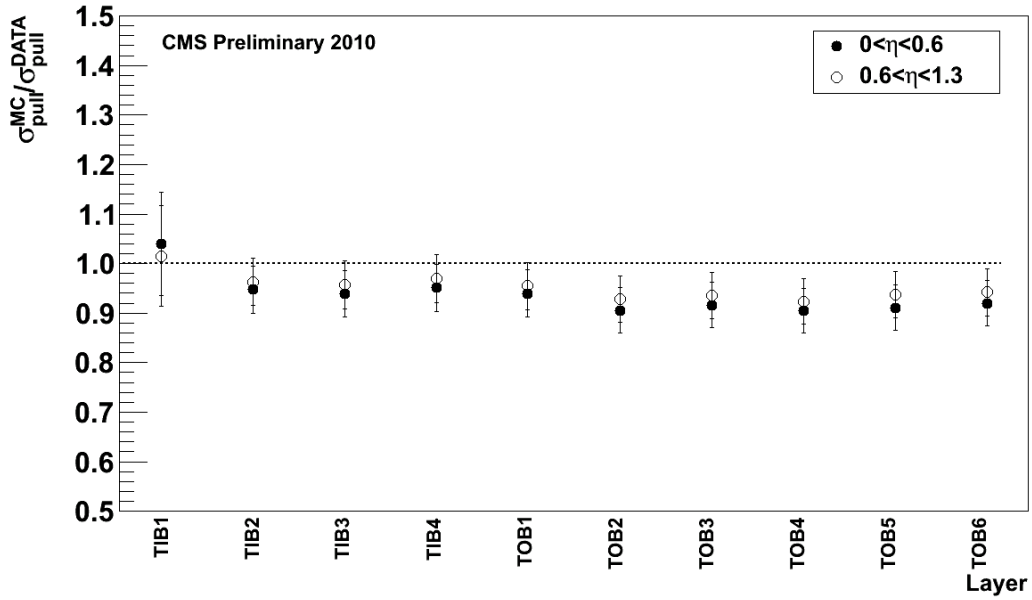

Figure 26: Ratio of the σ_i^{pull} values obtained on simulation and data for the barrel planes. The detection layers on the x-axis are the destination layers.

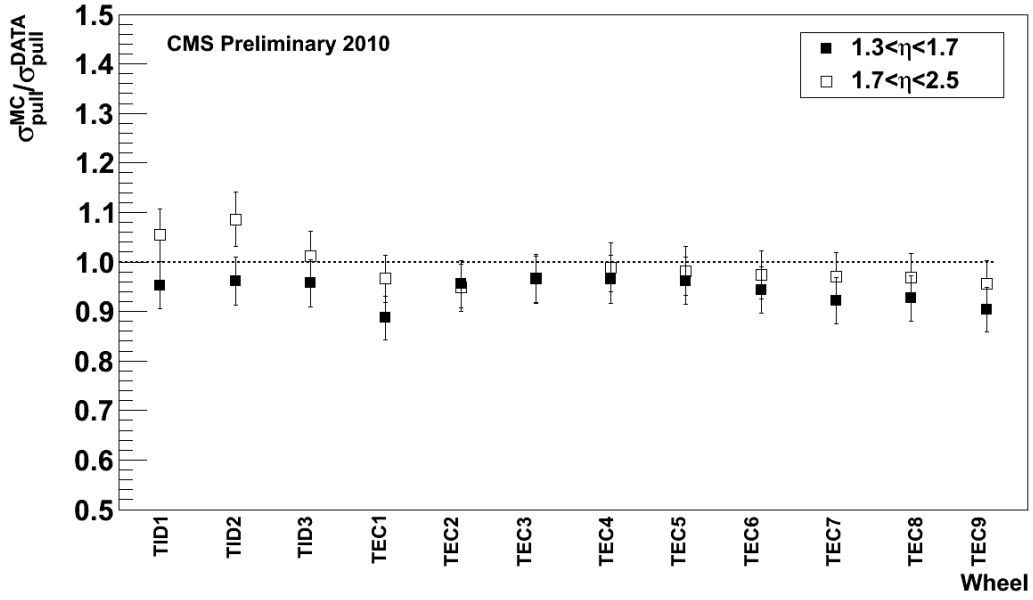

Figure 27: Ratio of the σ_i^{pull} values obtained on simulation and data for the endcap planes. The detection layers on the x-axis are the destination layers.

The information obtained with these techniques can be used to give feedback for evaluation of Tracker material related systematic uncertainties to physics analyses, and to further improve both the details of the simulation of the material inside the tracking volume, as well as the treatment of material effects in the track reconstruction model.

References

[1] CMS Collaboration, "The CMS experiment at the CERN LHC", *JINST* **0803** (2008) S08004. doi:10.1088/1748-0221/3/08/S08004.

[2] CMS Collaboration, "Tracking and Vertexing Results from First Collisions", *CMS Physics Analysis Summary* **TRK-10-001** (2010).

[3] GEANT4 Collaboration, "GEANT4: A simulation toolkit", *Nucl. Instrum. Meth.* **A506** (2003) 250–303. doi:10.1016/S0168-9002(03)01368-8.

[4] J. Allison et al., "Geant4 developments and applications", *IEEE Transaction on Nuclear Science* **53 No.1** (2006) 270.

[5] R. Ranieri, "The Simulation of the CMS Silicon Tracker", *CMS Conference Report* **2008/007** (2007).

[6] E. Migliore and G. Sguazzoni, "Altered scenarios of the CMS Tracker material for systematic uncertainties studies", *CMS Note* **2010/010** (2010).

[7] T. Sjostrand, S. Mrenna, and P. Z. Skands, "PYTHIA 6.4 Physics and Manual", *JHEP* **05** (2006) 026, arXiv:hep-ph/0603175.

[8] A. J. Bell, "The design and construction of the beam scintillation counter for CMS", Master's thesis, University of Canterbury, Christchurch, New Zealand, 2008. CERN-THESIS-2009-062.

[9] T. Aumeyr, "Beam phase and intensity monitoring for the Compact Muon Solenoid experiment", Master's thesis, Vienna University of Technology, Vienna, Austria, 2008.

[10] N. Marinelli, "Track finding and identification of converted photons", *CMS Note* **2006/005** (2006).

[11] CMS Collaboration, "Photon reconstruction and identification at $\sqrt{s}$=7TeV", *CMS Physics Analysis Summary* **CMS-PAS-EGM-10-005** (2010).

[12] S. Wasserbaech, "Computeraized tomography of the ALEPH detector", *ALEPH Internal Note* **ALEPH 97-08** (1997).

[13] CMS Collaboration, "Alignment of the CMS Silicon Tracker during Commissioning with Cosmic Rays", *JINST* **5** (2010) T03009, arXiv:0910.2505. doi:10.1088/1748-0221/5/03/T03009.